

Modeling of selfelectroopticeffect devices

P. J. Mares and S. L. Chuang

Citation: *J. Appl. Phys.* **74**, 1388 (1993); doi: 10.1063/1.354897

View online: <http://dx.doi.org/10.1063/1.354897>

View Table of Contents: <http://jap.aip.org/resource/1/JAPIAU/v74/i2>

Published by the [American Institute of Physics](#).

Related Articles

Plasmon-induced local photocurrent changes in GaAs photovoltaic cells modified with gold nanospheres: A near-field imaging study

J. Appl. Phys. **110**, 104306 (2011)

Photodiode with nanocrystalline Si/amorphous Si absorber bilayer

Appl. Phys. Lett. **99**, 191111 (2011)

Response to "Comment on 'Resilience of gated avalanche photodiodes against bright illumination attacks in quantum cryptography'" [*Appl. Phys. Lett.* **99**, 196101 (2011)]

Appl. Phys. Lett. **99**, 196102 (2011)

Full-band Monte Carlo simulation of high-energy carrier transport in single photon avalanche diodes:

Computation of breakdown probability, time to avalanche breakdown, and jitter

J. Appl. Phys. **110**, 084507 (2011)

Ultra-low noise single-photon detector based on Si avalanche photodiode

Rev. Sci. Instrum. **82**, 093110 (2011)

Additional information on J. Appl. Phys.

Journal Homepage: <http://jap.aip.org/>

Journal Information: http://jap.aip.org/about/about_the_journal

Top downloads: http://jap.aip.org/features/most_downloaded

Information for Authors: <http://jap.aip.org/authors>

ADVERTISEMENT


AIPAdvances

Submit Now

**Explore AIP's new
open-access journal**

- **Article-level metrics
now available**
- **Join the conversation!
Rate & comment on articles**

Modeling of self-electro-optic-effect devices

P. J. Mares and S. L. Chuang

Department of Electrical and Computer Engineering, University of Illinois at Urbana-Champaign,
1406 West Green Street, Urbana, Illinois 61801

(Received 15 October 1992; accepted for publication 22 March 1993)

A detailed comparison is presented between a comprehensive theoretical model, which uses the linewidth as the only fitted parameter, and a consistent set of experimental data for (i) the electro-optical properties of quantum-well (QW) modulators and (ii) the input power versus output power characteristics of interband self-electro-optic-effect devices (SEEDs). The model, which is founded on basic principles, includes excitonic effects and employs the depletion approximation to relate the applied bias to the electric field and to phenomenologically approximate the internal quantum efficiency. It is shown that this model is able to emulate and predict the behavior of QW modulators and SEEDs very well.

I. INTRODUCTION

During the past few years multiple-quantum-well (MQW) structures have been extensively investigated. Multiple-quantum-well structures are of particular interest because, when an electric field is applied perpendicular to the MQWs, they can exhibit strong excitonic absorption near the band gap due to the quantum confined Stark effect (QCSE).¹⁻³ In contrast to bulk semiconductors, these excitonic peaks in MQWs are observed at room temperature and persist even when large electric fields are applied. Researchers have taken advantage of the QCSE to design a host of novel detectors and modulators which exhibit enhanced performance compared to bulk semiconductors. By far the greatest effort has been centered on the AlGaAs/GaAs system, although other material systems, most notably InGaAs/InP for 1.55 μm operation, have been the subject of much research.^{4,5}

Recently there has been much interest in optical devices for switching and processing applications because of the ability of optics to communicate large amounts of information in parallel. The self-electro-optic-effect device (SEED) is an optically bistable device that combines optics and electronics and can function as an optical switch.^{2,3} A SEED consists of a p - i - n diode with multiple quantum wells in the intrinsic region connected in series with a bias source and a load.^{3,6,7} The load may be a resistor (R-SEED), a constant current source, or an identical p - i - n diode with multiple quantum wells in the intrinsic region (S-SEED). The key to the SEED concept is a p - i - n diode, based on the QCSE, which functions simultaneously as a photodetector and as a modulator. Interband SEED devices employ the strong electroabsorption effects in QWs (QCSE) as a low-energy physical mechanism. The electrical energy, needed to alter the optical properties of the MQW structure, is essentially that required to charge up the volume of the device to the operating field. The speed of QCSE modulators is basically limited by the time it takes to apply the electric field to them. The versatility of the SEED concept is exemplified by its many different modes of operation. SEEDs can be employed as memory elements, optical level shifters, wavelength converters, self-

linearized modulators, oscillators, and sense amplifiers.^{3,6-11}

Due to the technological importance of quantum-well electro-optical modulators in general and, in particular, as the basic building blocks of SEEDs, we have undertaken to complete a theoretical model based on the approach of Miller *et al.*¹ and Kan *et al.*¹² It is shown in this article that this model can accurately emulate and predict, starting from basic principles, the behavior of quantum-well modulators and SEEDs. Although many authors have investigated various aspects of the physics of quantum-well structures, most studies were focused on exciton transition energies and/or the optical-absorption coefficient. We present a detailed comparison between theory and experiment, using the linewidth as the only fitted parameter, for (i) the electro-optical properties and (ii) the input power versus output power (input/output) characteristic of interband SEEDs based on a consistent set of experimental data from Refs. 2 and 3. The theoretical results agree very well with the experimental data. In Sec. II, we outline and present results for interband electroabsorption in MQW structures. Then, in Sec. III, the operation and modeling of interband SEED devices utilizing the QCSE are examined. Finally, Sec. IV contains our conclusions.

II. INTERBAND ELECTROABSORPTION

For electric fields applied perpendicular to MQWs, the QCSE¹ gives large electroabsorption near the band gap of QW semiconductors and is the basic physical mechanism behind most SEEDs. One effect of QWs is that the electrons and holes behave as if they were particles in a box and this confinement leads to discrete energy levels for the electrons and the holes perpendicular to the layers. As a result, the absorption spectrum breaks up into a "stair-case like" structure with different steps associated with transitions between different electron and hole subbands. In addition, strong absorption peaks are observed at the edges of this "staircase like" structure. In Sec. II A the electronic properties of MQW structures are examined, and in Sec. II B the optical properties of MQW structures are outlined.

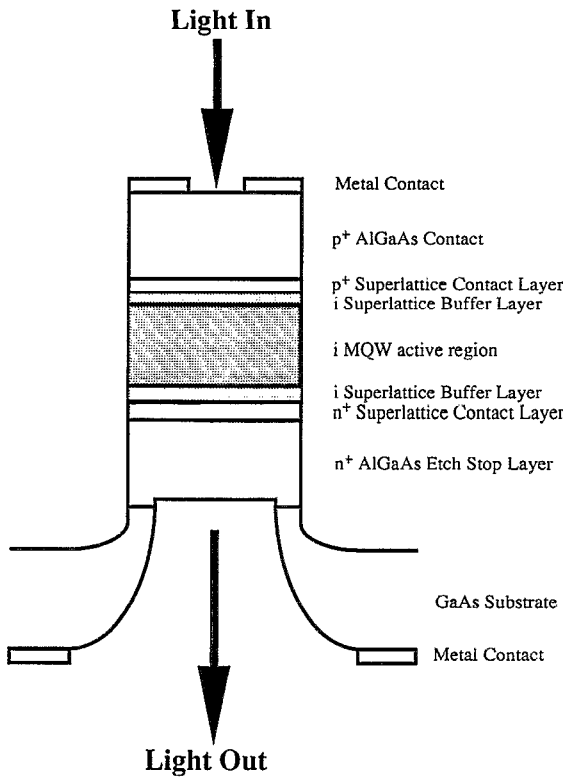


FIG. 1. A schematic representation of the sample structure in which the electric field was applied perpendicular to the MQWs (see Ref. 13). The intrinsic MQW active region consists of 50 periods of 95 Å GaAs quantum wells surrounded by 98 Å $\text{Al}_{0.32}\text{Ga}_{0.68}\text{As}$ barriers. The intrinsic superlattice buffers each consist of 30 periods of 29 Å GaAs layers alternating with 69 Å $\text{Al}_{0.32}\text{Ga}_{0.68}\text{As}$ layers. The sample was antireflection coated at the n^+ air/device interface.

A. Electronic properties

A schematic representation of one of the AlGaAs/GaAs MQW structures used by researchers at AT&T Bell Laboratories to investigate SEED devices is shown in Fig. 1. The MQW intrinsic region structure parameters, as experimentally expected after growth, are listed in the figure caption. For a MQW structure, the single-particle energies of electrons, heavy holes, and light holes can be found by solving

$$H_e \phi_e = E_e \phi_e \quad (1)$$

for electrons, and a similar equation with H_h , ϕ_h , and E_h for holes. The Hamiltonian for electrons H_e is

$$H_e = (P_{z_e}^2 / 2m_e^*) + V_e(z_e) + eFz_e, \quad (2)$$

while the Hamiltonian for holes H_h is

$$H_h = (P_{z_h}^2 / 2m_{hl}^*) + V_h(z_h) - eFz_h. \quad (3)$$

Above, $V_e(z_e)$ [$V_h(z_h)$] is the quantum-well confining potential for electrons (holes), F is the electric field perpendicular to the plane of the layers, z_e (z_h) is coordinate of the electron (hole) perpendicular to the plane of the layers, and P_{z_e} (P_{z_h}) is the momentum operator for the electron (hole). The heavy- and light-hole Hamiltonians differ

only in the definition of the effective mass (m_{hl}^*) used in Eq. (3). For the hole states, m_{hl}^* is given by

$$1/m_{hl}^* = (1/m_0)(\gamma_1 \mp 2\gamma_2), \quad (4)$$

where the upper (lower) sign refers to the heavy hole (light hole) effective mass. The valence-band Luttinger parameters, γ_1 and γ_2 , are used because they give a better approximation for the hole effective masses than using isotropic hole effective masses. The solutions to Eq. (1) can be found by modeling the wave functions $\phi_{e(h)}$ either as sums of exponentials using discretized step potentials or as Airy functions and subsequently using a propagation (or transfer) matrix technique. We have used both methods to compute the eigenvalues and the wave functions. The Airy functions are exact solutions to the Schrödinger equation with an applied electric field. However, when an interval spacing of $\Delta z < 2$ Å is used in the propagation matrix technique, there is no detectable difference between the eigenvalues and wave functions obtained using Airy functions and those obtained using sums of exponentials.

Since the active intrinsic region of Fig. 1 consists of MQWs separated by large barriers, the quantum wells are essentially decoupled and the structure can be modeled as a series of isolated single quantum wells. The best fit between experimental data and theory is obtained using a well width of 98 Å and a barrier width of 104 Å. For the GaAs quantum wells, we use $\gamma_1 = 6.79$ and $\gamma_2 = 1.92$.¹⁴ These Luttinger parameters yield hole effective masses of $m_{hh}^* = 0.34m_0$ and $m_{lh}^* = 0.094m_0$ which are identical to those of Miller *et al.*¹ The effective masses in the $\text{Al}_{0.32}\text{Ga}_{0.68}\text{As}$ barriers are modeled as¹

$$m_{hh}^* = (0.34 + 0.42x)m_0, \quad (5)$$

$$m_{lh}^* = (0.094 + 0.043x)m_0, \quad (6)$$

where x is the Al mole fraction in $\text{Al}_x\text{Ga}_{1-x}\text{As}$. The electron effective mass in the well as well as in the barrier is given by

$$m_e^* = (0.0665 + 0.0835x)m_0. \quad (7)$$

The confining potentials $V_e(z_e)$ and $V_h(z_h)$ are computed using

$$E_g = (1.426 + 1.247x) \text{ eV} \quad (8)$$

and a band offset ratio¹⁵ of $\Delta E_c / \Delta E_v = 67/33$. We also take into account the 4.5 meV built-in strain shift for the light-hole band since strain was found¹ to be present in the structure of Fig. 1. Using the above parameters, the C1, HH1, HH2, and LH1 single-particle energies for this quantum-well structure are shown in Fig. 2. The ground-state eigenvalues (C1, HH1, LH1) drop deeper into their respective quantum wells with applied electric field. The rate at which the ground-state eigenvalues red shift increases with applied electric field. The ground-state single-particle energies shift at similar rates with the HH1 eigenvalue red shifting at a slightly faster rate than the LH1 eigenvalue which, in turn, red shifts slightly faster than the C1 eigenvalue.

The continuum transition energy for absorption between the valence band and the conduction band is computed from

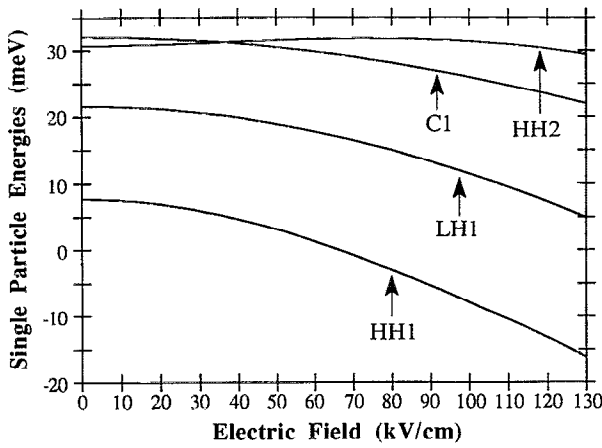


FIG. 2. Theoretical single-particle energies for the MQW structure shown in Fig. 1.

$$E_{eh} = E_g + E_e + E_h, \quad (9)$$

where E_g is the quantum-well band-gap energy, E_e is the electric-field-dependent conduction-band eigenvalue, while E_h is the electric-field-dependent heavy-hole or light-hole single-particle energy; however, in quantum wells, excitons dominate the features of the absorption spectrum. Consequently, to model the electroabsorption in quantum wells properly, excitonic effects must be included. The exciton (bound state) transition energy lies just below the continuum transition energy by an amount equal to the binding energy E_B and is given by

$$E_{ch} = E_g + E_e + E_h + E_B. \quad (10)$$

In computing the binding energy, the effective mass approximation is used, and band nonparabolicity is neglected. After a transformation into center of mass coordinates, the exciton Hamiltonian becomes^{1,16}

$$H_{ex} = H_e + H_h - \frac{\hbar^2 \nabla_\rho^2}{2\mu} - \frac{\hbar^2 \nabla_R^2}{2(m_e + m_{h\parallel})} - \frac{e^2}{4\pi\epsilon_r\epsilon_0 \sqrt{\rho^2 + (z_e - z_h)^2}}. \quad (11)$$

The Hamiltonian H_e (H_h) depends on electric field and is given by Eq. (2) [Eq. (3)]. Above, ρ is the in-plane separation vector between the electron and hole ($\rho = \mathbf{r}_{e\parallel} - \mathbf{r}_{h\parallel}$), \mathbf{R} is the position vector of the center of mass in the transverse plane, and ϵ_r is the relative dielectric constant. The third term in Eq. (11) corresponds to the reduced exciton motion and is the kinetic-energy term of the electron and hole relative motion. The reduced effective mass in the plane of the layers μ is given by

$$1/\mu = (1/m_e^*) + (1/m_{h\parallel}), \quad (12)$$

where $m_{h\parallel}$, the hole effective mass in the plane of the layers, is calculated from

$$1/m_{h\parallel} = (1/m_0)(\gamma_1 \pm \gamma_2). \quad (13)$$

Here, the upper (lower) sign corresponds to the heavy (light) hole. The fourth term in Eq. (11) is the kinetic energy term for the center-of-mass motion. Since optical absorption comes from excitons with a total in-plane momentum $\mathbf{K}_{\parallel} \cong 0$, the center-of-mass contribution is dropped from the discussion below. Finally, the last term in Eq. (11) is the Coulomb potential energy term. We are primarily interested in the 1S excitonic states since those are the ones generally observed in absorption spectra. A variational technique^{1,12} is employed to compute the binding energy.

The normalized separable 1S-like trial wave function is given by^{16,17}

$$\Psi_{ex}(z_e, z_h, \rho) = \phi_e(z_e) \phi_h(z_h) \phi(\rho), \quad (14a)$$

$$\phi(\rho) = \sqrt{2/\pi} (e^{-\rho/\lambda}/\lambda). \quad (14b)$$

Here, λ is the variational parameter and the exponential term in Eq. (14b) is used to model the in-plane behavior of the exciton wave function. The wave functions $\phi_e(z_e)$ and $\phi_h(z_h)$ are obtained by solving Eqs. (1)–(3) and have, respectively, eigenvalues E_e and E_h . Using Eq. (14), the binding energy is determined by minimizing

$$\langle \Psi_{ex} | H_{ex} | \Psi_{ex} \rangle = E_e + E_h + E_B(\lambda), \quad (15a)$$

with respect to λ ,^{1,16} where

$$E_B(\lambda) = \frac{\hbar^2}{2\mu\lambda^2} - \frac{e^2}{4\pi\epsilon_r\epsilon_0} \times \int_{-\infty}^{\infty} dz_e \int_{-\infty}^{\infty} dz_h |\phi_e(z_e)|^2 |\phi_h(z_h)|^2 \times \int_0^{\infty} dq \frac{e^{-q|z_e - z_h|}}{[1 + (\lambda q/2)^2]^{3/2}}. \quad (15b)$$

To find the binding energy, for each value of the variational parameter which is assumed, the integral over \mathbf{q} must be repeatedly evaluated for every value of z_e and z_h . As a result, this minimization procedure can be computationally time consuming. However, the integral over \mathbf{q} can be rewritten as

$$\int_0^{\infty} dq \frac{e^{-q|z_e - z_h|}}{[1 + (\lambda q/2)^2]^{3/2}} = \left(\frac{2}{\lambda}\right) G\left(\frac{2|z_e - z_h|}{\lambda}\right), \quad (16)$$

where $G(x)$ is defined explicitly in the Appendix. The function $G(x)$ can be expressed in the following equivalent forms:

$$\int_0^{\pi/2} d\theta \cos \theta e^{-x \tan \theta}, \quad (17a)$$

$$x\{(\pi/2)[H_1(x) - N_1(x)] - 1\}, \quad (17b)$$

$$\text{polynomial approximation (see Appendix)}. \quad (17c)$$

Above $H_1(x)$ is the first-order Struve function and $N_1(x)$ is the first-order Neumann function. Although the form in Eq. (17b) is an improvement over the integral that must be computed in Eq. (17a), we find that our polynomial approximation (see Appendix) for the function $G(x)$ significantly improves the speed of the computation for the bind-

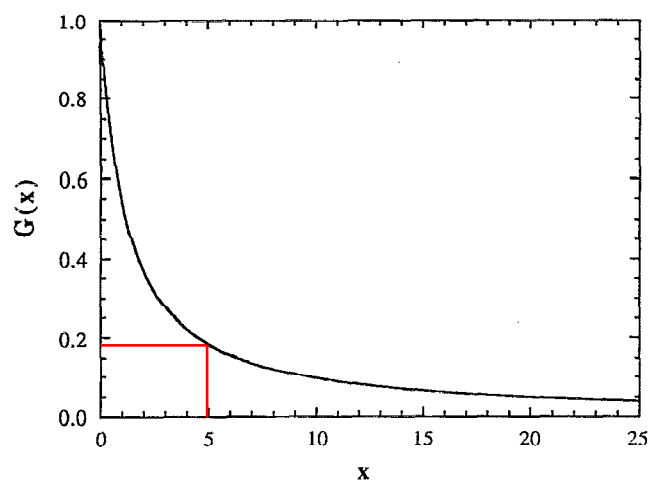


FIG. 3. The function $G(x)$ [Eq. (16)] plotted using the three methods of Eq. (17). The three expressions of Eq. (17) yield identical results and consequently only a single line appears. This demonstrates that there is no loss of accuracy when the polynomial approximation [Eq. (17c)] is adopted in the computation of the binding energies.

ing energies. The function $G(x)$ is plotted in Fig. 3 using the three expressions in Eq. (17). In Fig. 3 only a single line appears demonstrating that all three expressions yield identical results and that there is no loss of accuracy when the polynomial approximation is adopted. In fact, the polynomial approximation [Eq. (17c)] deviates from the exact solution [Eq. (17a)] by less than 1% for all x except in a very small region around $x=6.5$ where the deviation is less than 1.5%.

Using the technique outlined above, we plot in Fig. 4 the binding energies versus electric field [Fig. 4(a)] and the mean in-plane extension of the exciton wave function,

$$\langle \rho \rangle = \langle \Psi_{\text{ex}} | \rho | \Psi_{\text{ex}} \rangle = \lambda, \quad (18)$$

as a function of electric field [Fig. 4(b)]. The parameter λ is the variational parameter in the exciton trial wave function of Eq. (14). With applied electric field, the HH1 and LH1 binding energies decrease in magnitude. This can be explained as follows. When a photon is absorbed, it creates an electron in the conduction band and a hole in the valence band. With applied electric field perpendicular to the layers, the electron is pulled to one side of the quantum well while the hole is pulled to the opposite side of the quantum well. Consequently, the attraction of the electron-hole pair is weakened and its average in-plane extension, described by the variational parameter λ [Fig. 4(b)], increases (i.e., its orbit becomes larger). However, the quantum-well barriers prevent the escape of the electron and hole from the quantum well and thus rapid field ionization is prevented. As a consequence excitons can be observed even at large electric fields. With increasing electric field, the HH2 binding energy at first increases and subsequently begins to decrease for large electric fields. At zero electric field the electron and hole are initially somewhat spatially separated and hence the HH2 binding energy is smaller than the HH1 binding energy where the electron and hole are primarily located in the same region

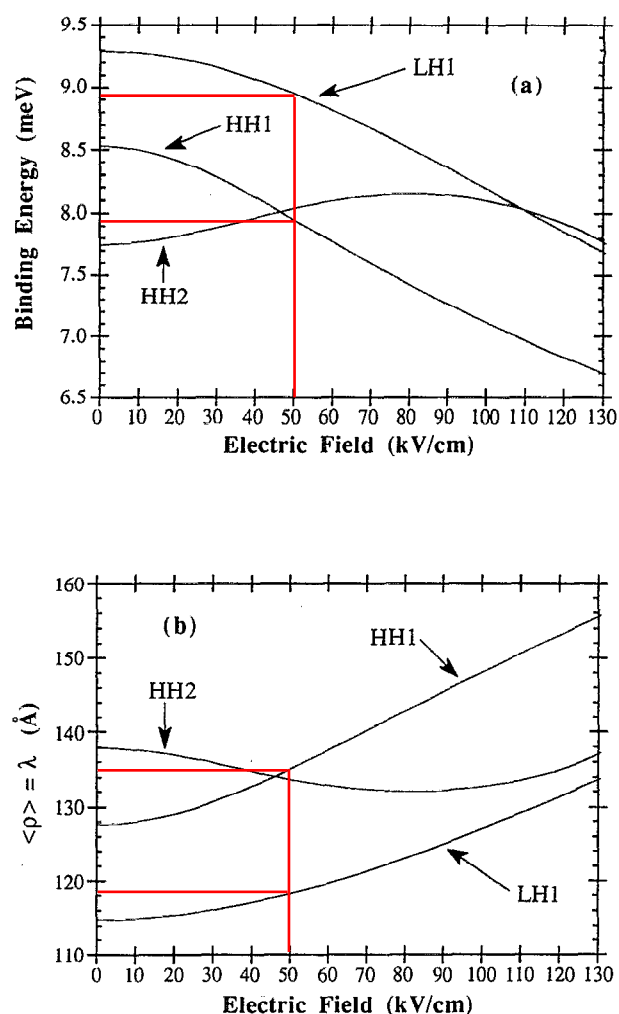


FIG. 4. Theoretical (a) binding energies and (b) mean in-plane extension of the exciton wave function as a function of electric field for the structure shown in Fig. 1.

of the quantum well. As the electric field becomes larger, the electron and hole are increasingly more located in the same region of the quantum well (near the side of the quantum well where the potential energy is lower). As a result, the Coulomb attraction becomes larger and the binding energy increases. At very high electric fields, due to the smaller effective mass of the electron, the electron is pulled closer to the barrier than is the hole, due to its large effective mass (i.e., the electron wave function leaks more into the barrier than does the HH2 wave function). Consequently, the attraction of the electron-hole pair is weakened. Therefore, at very large electric fields, the HH2 binding energy begins to decrease.

For the structure of Fig. 1, the transition energies are displayed in Fig. 5 where the solid lines and dashed lines represent, respectively, the exciton and subband-edge (continuum) transition energies. Excellent agreement is obtained between our theoretical results (solid lines) and the experimental data (crosses and open circles) of Miller *et al.*¹ Figure 5 shows that the transitions red shift displaying the well-known quadratic behavior with applied elec-

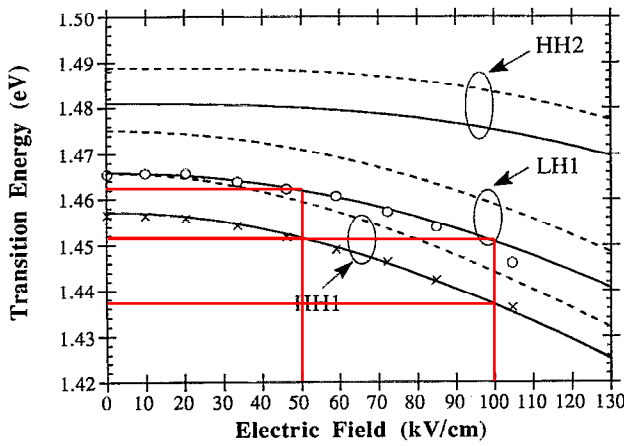


FIG. 5. Theoretical bound and continuum transition energies for transitions between the HH1, HH2, and LH1 states in the valence band and the ground state in the conduction band. The solid lines correspond to the exciton transition energies while the dashed lines represent the transition energies of the continuum. The crosses and open circles are experimental results from Ref. 1 for the HH1 and LH1 exciton transition energies, respectively. The experimental error (obtained from Ref. 1) was 1.5 meV at low electric fields and 4.0 meV at 100 kV/cm.

tric field. At higher electric fields the transition energies shift at a faster rate than they do at low electric fields. The HH1 and LH1 exciton transition energies move at similar rates with the HH1 exciton transition energy moving slightly more than the LH1 exciton transition energy, especially at large electric fields. The dominant contribution to the red shifting of the exciton transition energies comes from the shift of the single particle energies (Fig. 2). This occurs because an electric field applied perpendicular to the plane of the layers directly affects the eigenvalues since the quantization is in the same direction as the applied electric field. However, the binding energies, which are an

indicator of the in-plane electron-hole binding, are only weakly affected by the same applied electric field (the exciton binding energies [Fig. 4(a)] change by less than 2 meV over the range of electric field investigated). Consequently, the primary effect of an electric field applied perpendicular to the plane of the layers is to cause a red shift of the exciton absorption peaks (Fig. 5).

B. Optical properties

To obtain good agreement, for absorption spectra of quantum-well structures, between experimental results and a theoretical model, the theoretical model must account for both the continuum and the exciton transitions. For a transition between two states $|a\rangle$ and $|b\rangle$, the interband absorption coefficient, based on the one electron-density matrix formulation, is given by¹⁸

$$\alpha(\omega) = \frac{2\omega}{n_r \epsilon_0 V} \sum_{\vec{k}_a} \sum_{\vec{k}_b} \frac{|M_{ab}|^2 \Gamma(f_a - f_b)}{(E_b - E_a - \hbar\omega)^2 + \Gamma^2}. \quad (19)$$

Above, $|M_{ab}|^2$ is the interband matrix element which is proportional to the square of the electron-hole overlap integral ($|\langle b | \hat{\epsilon} \cdot \mathbf{e} r | a \rangle|^2$), $\hat{\epsilon}$ is the polarization vector, Γ is the half-linewidth, while f_a (f_b) is the Fermi Dirac distribution function of the initial (final) state $|a\rangle$ ($|b\rangle$). For an undoped well, $f_a = 1$ and $f_b = 0$. The symbols E_a and E_b represent the total energy of the initial and final states, respectively, while n_r is the refractive index, c is the speed of light, and ϵ_0 is the permittivity of free space. The factor of 2 in Eq. (19) comes from the summation over spin. With the appropriate matrix elements, Eq. (19) can be used to model both the continuum and the bound parts of an interband transition.

After carrying out the summations in Eq. (19) and making use of some variable transformations, the absorption coefficient for continuum interband transitions is given by

$$\alpha(\omega) = \frac{\omega \mu e^2}{n_r \epsilon_0 \pi m_0^2 L_p} \sum_m \sum_n |I_{nm}|^2 |M_{AVG}|^2 \int_0^\infty \frac{dE M(E) S_{nm} \Gamma}{(E_g + E_m + E_n + E)^2 [(E_g + E_m + E_n + E - \hbar\omega)^2 + \Gamma^2]}, \quad (20)$$

where

$$I_{nm} = \langle \phi_n(z) | \phi_m(z) \rangle, \quad (21)$$

$$|M_{AVG}|^2 = \frac{m_0}{6} \left(\frac{m_0}{m^*} - 1 \right) \frac{E_g(E_g + \Delta)}{[E_g + (2\Delta/3)]}. \quad (22)$$

The sum over m (n) is over the valence (conduction) subbands. Here, E_m (E_n) is the single-particle energy of the m th hole (n th electron) subband with corresponding wave function $\phi_m(z)$ [$\phi_n(z)$]. Above, E_g is the band-gap energy, Δ is the spin-orbit split-off energy, L_p is the length of one period of the quantum-well structure, m_0 is the rest mass of an electron, and μ is the reduced effective mass given by Eq. (12). The symbol I_{nm} stands for the electron-hole overlap integral, S_{nm} is the Coulomb or Sommerfeld enhancement factor, and $|M_{AVG}|^2$ is the average matrix element for the Bloch state. The energy- and polarization-dependent matrix element $M(E)$ is obtained from the Kane model^{12,19,20} and is given in Table I for TE and TM polarizations.

The contribution to the total absorption coefficient due to bound (exciton) transitions can also be obtained by starting with Eq. (19). For bound transitions between the subbands $|m\rangle$ and $|n\rangle$, the exciton absorption coefficient is given by

TABLE I. Energy and polarization dependent matrix elements, $M(E)$, appearing in Eqs. (20) and (23). The variables E_m and E_n are, respectively, the single particle energies of the hole and the electron involved in the transition from state m to state n . The symbol E is the integration variable in Eq. (20).^{12,19,20}

	Continuum transitions		Exciton transitions	
	TE	TM	TE	TM
Heavy holes	$\frac{3}{4}\left[1+\left[\frac{E_m+E_n}{E_m+E_n+E}\right]\right]$	$\frac{3}{2}\left[1-\left[\frac{E_m+E_n}{E_m+E_n+E}\right]\right]$	$\frac{3}{2}$	0
Light holes	$\frac{1}{4}\left[5-3\left[\frac{E_m+E_n}{E_m+E_n+E}\right]\right]$	$\frac{1}{2}\left[1+3\left[\frac{E_m+E_n}{E_m+E_n+E}\right]\right]$	$\frac{1}{2}$	2

$$\alpha(\omega)=\frac{2\omega e^2\hbar^2}{n_r\epsilon\epsilon_0m_0^2L_p}\sum_{mn}\frac{M(E)|M_{\text{AVG}}|^2|I_{nm}|^2|\phi(\rho=0)|^2\Gamma}{(E_g+E_m+E_n+E_B)^2[(E_g+E_m+E_n+E_B-\hbar\omega)^2+\Gamma^2]}.\tag{23}$$

Here, E_B is the binding energy [Eq. (15)], $M(E)$ is the energy- and polarization-dependent matrix element given in Table I, and $\phi(\rho)$ is the normalized exciton trial wave function [Eq. (14b)]. It has recently been found²¹ that in AlGaAs/GaAs quantum-well structures to properly model the average matrix element for the Bloch states $|M_{\text{AVG}}|^2$ [Eq. (22)], the effective mass m^* that must be used in Eq. (22) is actually smaller ($m^*=0.053m_0$) than the measured effective mass ($m^*=0.0665m_0$). Consequently, if the measured effective mass is used in Eq. (22) then, to account for the effect of the other bands on the curvature of the conduction band, the continuum and bound absorption coefficients [Eqs. (20) and (23)] must be multiplied by a factor of 1.27.

For the MQW p - i - n structure of Fig. 1, with the electric field applied perpendicular to the quantum wells, the theoretically computed absorption spectrum is shown in Fig. 6. It is obtained using a field-dependent linewidth which is based upon the results of Cho and Prucnal.²² For

example, the half-linewidth varies from 3.32 meV at $F=0$ kV/cm to 5.0 meV at 160 kV/cm. The relation between the applied electric field and the applied bias is determined via the depletion approximation accounting for the finite background doping in the intrinsic region. In addition to the parameter values cited above, we use an optical dielectric constant of $\epsilon_{\text{opt}}=11.549$, a spin-orbit split-off energy of $\Delta=0.34$ eV, and constant Coulomb enhancement factors of 1.4 and 1.6, respectively, for the heavy-hole and light-hole transitions. This Coulomb enhancement factor is equivalent to an average of a pure 2D enhancement factor which equals 2 at the band edge and approaches 1 monotonically as E approaches infinity. For a given applied bias, two absorption peaks are observed. For this material system (AlGaAs/GaAs), the peak lying lower in energy corresponds to the heavy-hole exciton while the second peak corresponds to the light-hole exciton. It is clear from Fig. 6 that the exciton peaks remain resolved to very high electric fields ($V=-17$ V is approximately 115 kV/cm when the built-in potential is 1.74 V). With increasing electric field applied perpendicular to the quantum wells, the exciton peaks red shift and the absorption decreases in magnitude. This behavior of the exciton peaks can be understood as follows. With applied electric field, for the ground states, the electron and hole move to opposite sides of the quantum well and, therefore, the overlap integral of the electron and hole wave functions decreases. Due to this electron-hole separation, the spatial extent of the exciton wave function $\langle\rho\rangle=\lambda$ in Fig. 4(b), increases. Consequently, the absorption coefficient, which is (i) proportional to the square of the electron-hole overlap integral and (ii) inversely proportional to the square of the variational parameter λ , decreases in magnitude with increasing electric field. The red shift of the exciton absorption spectrum is due primarily to the shift of the single-particle energies. This shift in transition energies and change in absorption coefficient magnitude, referred to as the QCSE, is the cornerstone of many novel modulators.

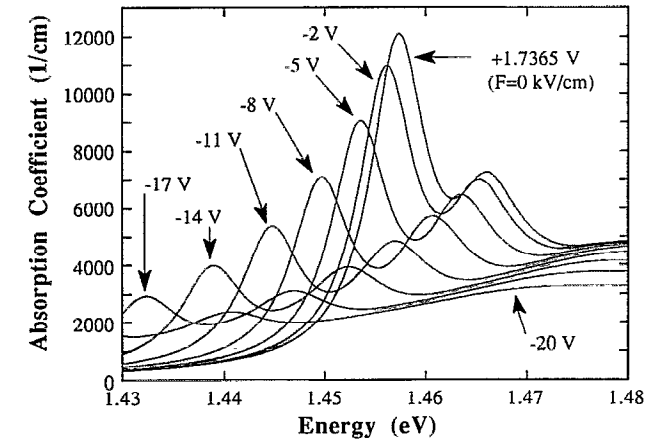


FIG. 6. The absorption spectrum for the structure of Fig. 1 at several bias voltages. The relation between the applied bias and the electric field is computed using the depletion approximation taking into account a constant background doping in the intrinsic region.

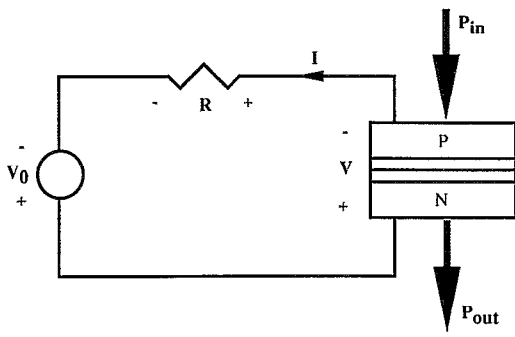


FIG. 7. The circuit for a resistor SEED (R-SEED).

III. OPERATION OF INTERBAND SEED

Interband SEED devices consist of a MQW p - i - n diode connected in series with a bias source and a load. Initially, resistors were used for the load (R-SEED). However, in an effort to improve performance, current sources were employed and subsequently an identical MQW p - i - n diode was used (S-SEED). Recently, a self-biased SEED (one that requires no external bias source) suitable for two-dimensional integration was demonstrated.²³

The initial SEED proposed by Miller *et al.*² consists of a p - i - n diode (with multiple quantum wells in the intrinsic region) connected in series with a bias source and a resistor. The key to the SEED concept is the p - i - n diode which functions simultaneously as a photodetector and as a modulator. The operation of SEED can be understood as follows.³ The electrical circuit is responsible for the manner in which a change in photocurrent modulates the voltage across the device. However, it is the photocurrent, which results from light incident upon the device, passing through the electronic circuit which changes the voltage across the modulator. The voltage across the modulator then affects the absorption of light by the modulator which in turn causes the photocurrent to be changed. Consequently, an optoelectronic feedback is established because without light incident on the device there is no optical absorption, thus no photocurrent, and hence no change in voltage across the device. The feedback mechanism is based on having a material which will absorb progressively more of the incident light when progressively more excited by the incident light.²⁴ Consequently, a positive feedback is established which can lead to switching under the proper conditions. This form of optical bistability does not depend on external optical feedback such as cavities or mirrors.

To characterize the operation of a R-SEED (circuit in Fig. 7) it is necessary to simultaneously solve the following two equations:

$$I(V) = P_{in} S(V), \quad (24)$$

$$I(V) = (V_0 - V)/R, \quad (25)$$

where the dark current is ignored for simplicity. The dark current is important only when a forward bias case is considered. In Eqs. (24) and (25), P_{in} is the input power on

the MQW p - i - n diode, V_0 is the bias voltage of the R-SEED circuit, and $S(V)$ is the current responsivity of the MQW p - i - n diode given by

$$S(V) = q\eta_{int} P_A / \hbar\omega, \quad (26)$$

$$P_A = (1 - r_p)(1 - e^{-\alpha L}) \left(\frac{1 + r_n e^{-\alpha L}}{1 - r_p r_n e^{-2\alpha L}} \right). \quad (27)$$

Here, q is the charge of an electron and P_A is the amount of power absorbed in the MQW p - i - n diode accounting for multiple reflections (this is an improvement over the commonly used single-pass result). For highly absorptive material the phase information is ignored.²⁵ Also, η_{int} is the internal quantum efficiency, r_p (r_n) is the reflectivity of the air/device interface at the p (n) doped region, while α and L are, respectively, the total absorption coefficient and the total length of the absorbing region in the MQW p - i - n diode. For normal incidence, the reflectivity of the air/device interface is

$$r_{p(n)} = \left(\frac{1 - \sqrt{\epsilon_{p(n)}}}{1 + \sqrt{\epsilon_{p(n)}}} \right)^2, \quad (28)$$

where $\epsilon_{p(n)} = \epsilon_p$ or ϵ_n is the dielectric constant of the p (n) doped region. The internal quantum efficiency is approximated, using the depletion approximation, as the ratio, at a given bias, of the length of the intrinsic region of the p - i - n MQW diode which is depleted, relative to the total length of the MQW p - i - n diode intrinsic region. In the intrinsic region, we account for the unintentional constant background doping. For applied bias values greater than that necessary to deplete the intrinsic region, our model assumes unity internal quantum efficiency. Using this method, for the structure of Fig. 1, the theoretically computed internal quantum efficiency reaches unity at a reverse bias of 2 V as was also determined, by Ref. 2, from experimental results. As a result, we believe this model to be a good approximation for the internal quantum efficiency. Equation (24) comes from a description of the current in the modulator as a function of the voltage across the modulator, the optical input power, and the energy of the incident light, while Eq. (25) describes the behavior of the circuit to which the modulator is connected. The theoretically computed responsivity for the structure of Fig. 1, which was antireflection coated at the n^+ air/device interface ($r_n = 0$), is shown in Fig. 8(a). The operating wavelength is 851.7 nm (~ 1.4568 eV) which corresponds to the zero-bias HH1 exciton peak. To obtain the results shown in Fig. 8(a), the αL product is modeled as

$$\alpha L = \alpha_{MQW} L_{MQW} + \alpha_R L_R, \quad (29)$$

where α_{MQW} (L_{MQW}) is the total absorption coefficient (length) of the MQW intrinsic region and α_R (L_R) is the residual absorption coefficient (length) of the remainder of the p - i - n diode. The total absorption coefficient α_{MQW} is shown in Fig. 6, while $\alpha_R \approx 380/\text{cm}$ is assumed. The residual absorption is included to account for the residual absorption inherently present in these structures. Very good agreement is obtained between our theoretical result [dashed line in Fig. 8(a)] and the experimental data of

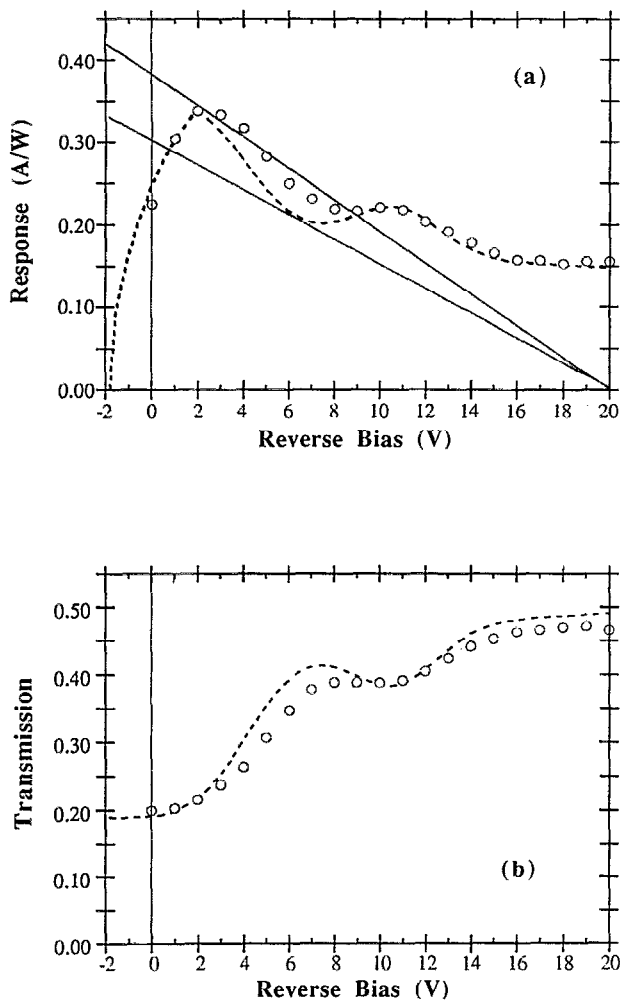


FIG. 8. (a) The theoretical (dashed line) and experimental (\circ) response vs applied reverse bias, for the structure of Fig. 1, at 851.7 nm (1.4568 eV). The solid lines are the load lines of the circuit for two representative input powers. (b) The theoretical (dashed line) and experimental (\circ) transmission vs applied reverse bias. The experimental data were obtained from Ref. 2.

Miller *et al.*² [open circles in Fig. 8(a)]. It is useful to recast the equations necessary to describe the operation of a SEED in terms of the responsivity of the MQW p - i - n diode [Eq. (26)] and the responsivity of the circuit to which the modulator is connected, i.e.,

$$S(V) = (V_0 - V) / P_{in} R. \quad (30)$$

A load line analysis, where Eq. (30) is the load, can be used to explain the operation of a SEED. Bistability is achieved when the response curve of the p - i - n diode [dashed line in Fig. 8(a)] and that of the load [solid lines in Fig. 8(a)] have three intersection points. Consequently, the bistable region exists for input powers such that the load line lies within the boundaries of the two load lines shown in Fig. 8(a). Having determined the input power, the corresponding output power is obtained from

$$P_{out} = T(V) P_{in}. \quad (31)$$

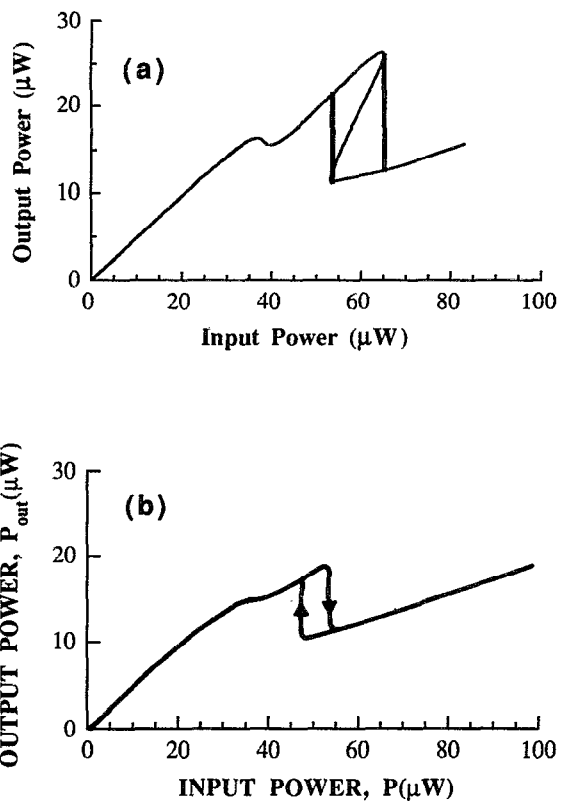


FIG. 9. (a) Theoretical R-SEED input/output characteristic, at 851.7 nm (1.4568 eV), for the structure of Fig. 1 with a 20 V bias source and a 1 M Ω resistor. (b) The corresponding experimental results from Ref. 2.

The transmission through a p - i - n MQW diode structure, including multiple reflections, is

$$T(V) = \frac{(1-r_p)(1-r_n)e^{-\alpha L}}{1-r_p r_n e^{-2\alpha L}}. \quad (32)$$

The result, for the structure of Fig. 1, is shown in Fig. 8(b). A good match exists between our theoretical result [dashed line in Fig. 8(b)] and the experimental data of Miller *et al.*² [open circles in Fig. 8(b)].

The input/output characteristic is calculated by solving for the responsivity of the p - i - n diode at a given applied bias [Eq. (26)] and subsequently using this value in Eq. (30) to determine the input power. The output power, for this applied bias, is then obtained from Eq. (31) by making use of the transmission in Eq. (32). In this manner we produced the input/output characteristic at 851.7 nm (\sim 1.4568 eV) shown in Fig. 9(a) for a 20 V bias source with a 1 M Ω resistor. The corresponding experimental data from Ref. 2 is shown in Fig. 9(b). The S-shaped curve associated with optical bistability is clearly evident, and a very good agreement exists between our theoretical result and the experimental data. In Fig. 10(a), the theoretically generated input/output characteristics at 851.7 nm are shown for a 1 M Ω resistor and varying values of supply voltage V_0 . The corresponding experimental data³ appear in Fig. 10(b). The above theoretical model accurately describes the voltage-supply-dependent features of the input/output characteristic. At this wavelength, bistability exists

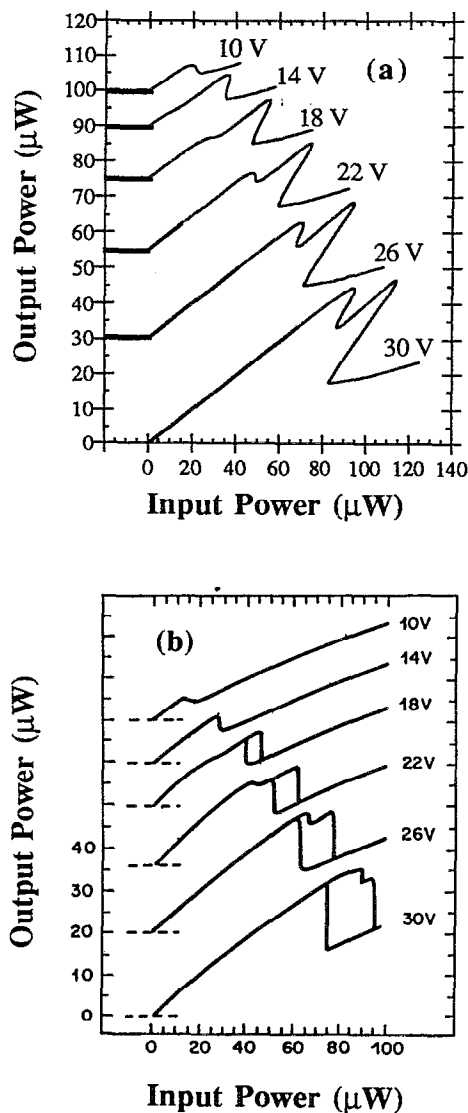


FIG. 10. (a) Theoretically computed input/output characteristics as a function of supply voltage V_0 . The R-SEED is operated at 851.7 nm (1.4568 eV) using a 1 M Ω resistor. (b) The corresponding experimental results from Ref. 3.

for all voltages in excess of 14 V. The small kink in the input/output characteristic immediately below the bistable region at low supply voltages is due to the light-hole exciton peak. For large supply voltages (> 22 V), this kink eventually develops into a second bistable region. This additional bistable loop is the result of multiple intersections between the load line and the responsivity curve of the MQW p - i - n diode. At large supply voltages, intersections can occur not only through the heavy-hole peak [near 3 V applied bias in Fig. 8(a)] but also through the light-hole peak [near 11 V applied bias in Fig. 8(a)]. In addition, the larger the supply voltage used the greater is the width of the bistable region. The width of the bistable region is primarily determined by the contrast in the maximum and minimum transmissions. From Fig. 8(b) it is evident that as the supply voltage is increased the contrast between the minimum and maximum transmissions improves. As a re-

sult, the width of the bistable region is greater when larger supply voltages are used.

IV. CONCLUSIONS

A comprehensive theoretical model, which is founded on the basic principles and uses the linewidth as the only fitted parameter, is outlined and is shown to successfully emulate and predict both the electrooptical properties of MQW modulators and the critical features of the input/output characteristic of SEEDs. Interband electroabsorption properties, including excitonic effects, are examined in the context of the density matrix approach and the Kane model. It is shown that our polynomial approximation can be used in the variational method, without loss of accuracy, to improve the speed of computation of the binding energies. A depletion approximation, which accounts for the finite background doping in the intrinsic region, is adopted to determine the relation between the applied bias and the electric field, and an empirical model is used to approximate the internal quantum efficiency of the p - i - n MQW modulator. Using the linewidth as the only fitted parameter, excellent agreement is obtained between the theoretical results and the experimental data^{1,2} for both the electronic and the optical properties of the MQW structure shown in Fig. 1. This is demonstrated by the very good agreement between theory and experiment for: (i) the exciton transition energies (Fig. 5); (ii) the responsivity [Fig. 8(a)]; and (iii) the transmission [Fig. 8(b)]. The operation of interband SEEDs based on the QCSE, the R-SEED in particular, was investigated. The above presented model can accurately reproduce the features of the input/output characteristic of SEEDs as is evidenced by the very good agreement that exists between our theoretical model and the experimental data^{2,3} (Figs. 9 and 10). This model will be very useful for predicting and optimizing the performance of both existing SEEDs and SEEDs based on future novel concepts and therefore in evaluating their applications to photonic circuits and smart pixels.

ACKNOWLEDGMENTS

The authors wish to thank D. A. B. Miller for helpful discussions. This work was supported partially by ONR under Grant No. N00014-90-J-1821 and by the Joint Service Electronics Program under Grant No. N00014-90-J-1270. Supercomputer time was supported by a grant from the National Center for Supercomputing Applications at the University of Illinois at Urbana-Champaign.

APPENDIX: POLYNOMIAL APPROXIMATION FOR THE FUNCTION $G(x)$

To reduce the computational bottleneck encountered when computing the binding energies, for the function $G(x)$ [Eq. (16)],

$$G(x) = \int_0^\infty dt \frac{e^{-xt}}{(1+t^2)^{3/2}}, \quad x > 0,$$

we developed the following polynomial approximation with a maximum error of less than 1.5%:

$$G(x) = \begin{cases} 1 + Ax + Bx^2 \ln\left(\frac{x}{2}\right) + Cx^2 + Dx^3 + Ex^4 \ln\left(\frac{x}{2}\right), & 0 < x \leq 6.8, \\ \frac{1}{x} - \frac{3}{x^3} + \frac{45}{x^5} - \frac{1575}{x^7}, & x > 6.8, \end{cases}$$

where

$$A = -8.9707 \times 10^{-1},$$

$$B = -2.5262 \times 10^{-1},$$

$$C = 2.2576 \times 10^{-1},$$

$$D = 3.2373 \times 10^{-2},$$

$$E = -4.1369 \times 10^{-4}.$$

Note that $G(0) = 1$. In the region $0 < x \leq 6.8$ the above fitting formula is employed. For arguments $x > 6.8$, the first four terms of the large argument expansion of Eq. (17b) are utilized.

¹D. A. B. Miller, D. S. Chemla, T. C. Damen, A. C. Gossard, W. Wiegmann, T. H. Wood, and C. A. Burrus, Phys. Rev. B **32**, 1043 (1985).

²D. A. B. Miller, D. S. Chemla, T. C. Damen, A. C. Gossard, W. Wiegmann, T. H. Wood, and C. Burrus, Appl. Phys. Lett. **45**, 13 (1984).

³D. A. B. Miller, D. S. Chemla, T. C. Damen, T. H. Wood, C. A. Burrus, A. C. Gossard, and W. Wiegmann, IEEE J. Quantum Electron. **QE-21**, 1462 (1985).

⁴I. Bar-Joseph, C. Klingshirn, D. A. B. Miller, D. S. Chemla, U. Koren, and B. I. Miller, Appl. Phys. Lett. **50**, 1010 (1987).

⁵S. Nojima, Y. Kawaguchi, K. Nakashima, and K. Wakita, Jpn. J. Appl. Phys. **26**, 1927 (1987).

⁶D. A. B. Miller, Opt. Quantum Electron. **22**, S61 (1990).

⁷D. A. B. Miller, Int. J. High Speed Electron. **1**, 19 (1990).

⁸A. L. Lentine, H. S. Hinton, D. A. B. Miller, J. E. Henry, J. E. Cunningham, and L. M. F. Chirovsky, IEEE J. Quantum Electron. **25**, 1928 (1989).

⁹A. L. Lentine, L. M. F. Chirovsky, L. A. D'Asaro, C. W. Tu, and D. A. B. Miller, IEEE Photon. Technol. Lett. **PTL-1**, 129 (1989).

¹⁰I. Bar-Joseph, G. Sucha, D. A. B. Miller, D. S. Chemla, B. I. Miller, and U. Koren, Appl. Phys. Lett. **52**, 51 (1988).

¹¹D. A. B. Miller, D. S. Chemla, T. C. Damen, T. H. Wood, C. A. Burrus, A. C. Gossard, and W. Wiegmann, Opt. Lett. **9**, 567 (1984).

¹²Y. Kan, H. Nagai, M. Yamanishi, and I. Suemune, IEEE J. Quantum Electron. **QE-23**, 2167 (1987).

¹³T. H. Wood, C. A. Burrus, D. A. B. Miller, D. S. Chemla, T. C. Damen, A. C. Gossard, and W. Wiegmann, Appl. Phys. Lett. **44**, 17 (1984).

¹⁴S. Nojima, Phys. Rev. B **37**, 9087 (1988).

¹⁵G. Ji, D. Huang, U. K. Reddy, H. Unlu, T. S. Henderson, and H. Morkoc, J. Vac. Sci. Technol. B **5**, 1346 (1987).

¹⁶J. A. Brum and G. Bastard, Phys. Rev. B **31**, 3893 (1985).

¹⁷G. Bastard, E. E. Mendez, L. L. Chang, and L. Esaki, Phys. Rev. B **26**, 1974 (1982).

¹⁸S. L. Chuang and D. Ahn, J. Appl. Phys. **65**, 2822 (1989).

¹⁹E. O. Kane, J. Phys. Chem. Solids **1**, 249 (1957).

²⁰M. Yamanishi and I. Suemune, Jpn. J. Appl. Phys. **23**, 35 (1984).

²¹R. H. Yan, S. W. Corzine, L. A. Coldren, and I. Suemune, IEEE J. Quantum Electron. **26**, 213 (1990).

²²H. Cho and P. R. Prucnal, IEEE J. Quantum Electron. **QE-25**, 1682 (1989).

²³K. W. Gossen, J. E. Cunningham, D. A. B. Miller, W. Y. Jan, A. L. Lentine, A. M. Fox, and N. K. Ailawadi, Quantum Optoelectronics: 1991 Technical Digest Series **7**, 26 (1991).

²⁴D. A. B. Miller, J. Opt. Soc. Am. B **1**, 857 (1984).

²⁵J. I. Pankove, *Optical Processes in Semiconductors* (Dover, New York, 1971).